Title

Multi-glycomic analysis of spheroid glycocalyx differentiates 2- and 3-dimensional cell models.

Journal

Glycobiology, 33(1)

Authors

Zhou, Qingwen
Solakyildirim, Kemal
Tena, Jennyfer
et al.

Publication Date

2023-01-08

DOI

10.1093/glycob/cwac075

Peer reviewed

Glycobiology, 2023, **33**, 1, 2–16
https://doi.org/10.1093/glycob/cwac075
Advance access publication date 8 November 2022
Original Article

Editor's Choice
Multi-glycomic analysis of spheroid glycocalyx differentiates 2- and 3-dimensional cell models

Qingwen Zhou[1], Michael Russelle S Alvarez[1,2], Kemal Solakyildirim[1,3], Jennyfer Tena[1], Luster Mae N Serrano[2], Matthew Lam[1], Cynthia Nguyen[1], Fernando Tobias[4], Amanda B Hummon[4], Ruel C Nacario[2], Carlito B Lebrilla[1,5,*]

[1]Department of Chemistry, University of California, Davis, CA, United States, [2]Institute of Chemistry, University of the Philippines Los Banos, Los Banos, Laguna, Philippines, [3]Department of Chemistry, Erzincan Binali Yildirim University, Erzincan, Turkey, [4]Department of Chemistry and Biochemistry, The Comprehensive Cancer Center, The Ohio State University, Columbus, OH, United States, [5]Department of Chemistry, Biochemistry, Molecular, Cellular and Developmental Biology Graduate Group, University of California, Davis, CA, United States
*Corresponding author: Department of Chemistry, University of California, Davis, CA, United States. Email: cblebrilla@ucdavis.edu

A multi-glycomic method for characterizing the glycocalyx was employed to identify the difference between 2-dimensional (2D) and 3-dimensional (3D) culture models with two human colorectal cancer cell lines, HCT116 and HT29. 3D cell cultures are considered more representative of cancer due to their ability to mimic the microenvironment found in tumors. For this reason, they have become an important tool in cancer research. Cell–cell interactions increase in 3D models compared to 2D, indeed significant glycomic changes were observed for each cell line. Analyses included the *N*-glycome, *O*-glycome, glycolipidome, glycoproteome, and proteome providing the most extensive characterization of the glycocalyx between 3D and 2D thus far. The different glycoconjugates were affected in different ways. In the *N*-glycome, the 3D cells increased in high-mannose glycosylation and in core fucosylation. Glycolipids increased in sialylation. Specific glycoproteins were found to increase in the 3D cell, elucidating the pathways that are affected between the two models. The results show large structural and biological changes between the 2 models suggesting that the 2 are indeed very different potentially affecting individual outcomes in the study of diseases.

Key words: 3D cell culture model; colon cancer; glycomics; mass spectrometry.

Introduction

Understanding the development and progression of cancer depends on models that closely recapitulate the disease. Conventional cancer research is performed on in vitro models, followed by in vivo models to validate the findings. The standard in vitro model for cancer is based on growing cultured cells on flat plates where the cells grow and expand into 2-dimensional (2D) space. However, the 2D model has limitations as a cancer model because it lacks certain elements found in tumors, namely artificial attachment of the cells, limited cellular interaction, and only formation of monolayers. On the other hand, in vivo models can mimic those elements, but in vivo methods are costly, time-consuming, and difficult to reproduce in similar in clinical trials (Lin and Chang 2008; Vidi et al. 2013). Therefore 3-dimensional (3D) cell culture models were developed to help bridge the gap between in vitro and in vivo studies.

Solid cancer tumors are by nature 3D with more extensive cell–cell interaction than 2D-grown cells. A 3D model can mimic the microenvironment and cell–cell interactions that are found in tumors (Katt et al. 2016). These provide better models for understanding cancer progression but also for testing cancer therapeutics. The 3D models are becoming more prevalent in cancer research and have been used for drug discovery to combat various types of cancers including colorectal, breast, and glioblastoma (Weigelt et al. 2014; Liu and Hummon 2015; Caragher et al. 2019).

Cell–cell interactions increase in the 3D compared to the 2D model. Thus, the glycocalyx, the highly interactive glycan-rich region of the cell membrane, could be significantly altered between 2D and 3D. The glycocalyx is a carbohydrate-rich environment found on the cell membranes composed of an array of glycolipids and glycoproteins, the latter with *N*- and *O*-glycans. The glycosylation of biomolecules is crucial for regulating several physiological and pathological functions, namely, immune response, protection against infection, and cell–cell interactions (Reily et al. 2019). Altered glycosylation is the hallmark of cancer, thus characterizing the changes associated with 2D versus 3D cell cultures would have important implications in the utility of the cancer model. Cancer-associated alterations in the glycocalyx include increased sialylation in proteins and lipids, increased core fucosylated *N*-glycans, and increased high-mannose glycans (de Leoz et al. 2011; Daniotti et al. 2013; Sethi and Fanayan 2015; Reily et al. 2019; Oh et al. 2021).

Various "omics" analyses have been performed to characterize the 3D models, including proteomic, lipidomic, phosphoproteomic, and metabolomic studies (Yue et al. 2016; Neef et al. 2020). These profiling methods give vital information regarding structural and biological functions. However, as the major changes between 2D and 3D cells is the extent of cell–cell interactions, an extensive analysis of the glycocalyx is essential but lacking. General interest in glycosylation has led to recent developments in new methods to characterize the glycocalyx particularly based on nano-liquid chromatography–mass spectrometry (nanoLC–MS) (Kailemia et al. 2018; Ruhaak et al. 2018). The high sensitivity of nanoflow allows the characterization of low abundance glycans, glycolipids, and glycoproteins in many biological systems (Zhou et al. 2021). This workflow employs mass analyzers

Received: August 4, 2022. **Revised:** September 10, 2022. **Accepted:** September 26, 2022

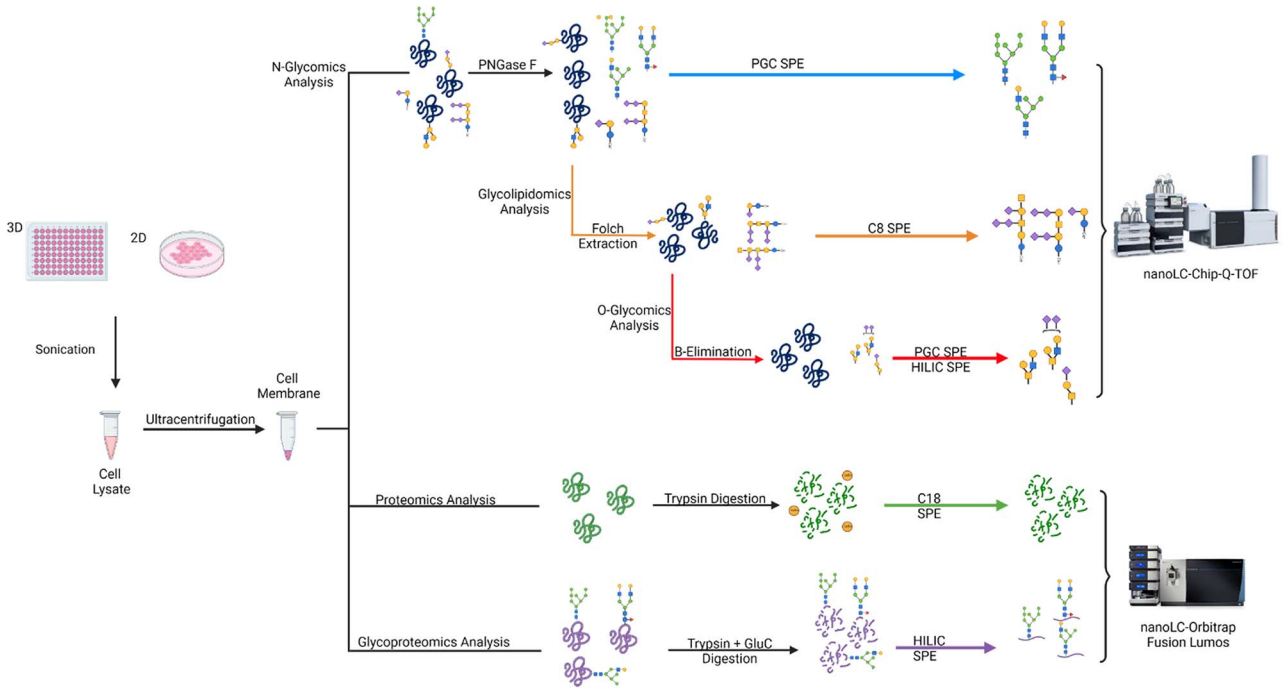

Fig. 1. The multi-glycomic workflow for the characterization of the glycocalyx in 2D and 3D cells of HCT116 and HT29. The membrane fractions were collected and further separated into 3 fractions. One was used for glycoproteomic, one for proteomic, and the last fraction for *N*-, *O*-glycomic and glycolipidomic analysis.

including quadrupole time-of-flight MS (nanoLC–QTOF MS) and an orbitrap MS (nanoLC–Orbitrap MS) to perform comprehensive analysis of glycans and their respective glycoconjugates.

In this work, we performed extensive multi-glycomic analysis of 2D and 3D cultured cell models in 2 human colorectal lines (HCT116 and HT29). The 2 cell lines were chosen because they contain commonly found mutations in colorectal cancer. HCT116 is a microsatellite instability cell line with a KRAS mutation, and HT29 is a microsatellite stable cell line with a p53 mutation (Duldulao et al. 2012). We examined simultaneously the *N*-glycome, *O*-glycome, glycolipidome, proteome, and glycoproteome revealing the differences between the 2 models using label-free glycomic quantification. In addition, a spatial *N*-glycomic profile was performed for the 3D model of both cell lines to determine glycosylation associated with the various layers of the 3D cells.

Results

The multi-glycomic procedure was adapted from a previously reported workflow (Li et al. 2020) and used for the comparative characterization of the 2D and 3D cell lines (Fig. 1). Briefly, it involved enrichment of the cell membrane that was then subjected to *N*-glycomics, *O*-glycomics, glycolipidomics, proteomics, and glycoproteomics analysis. For this study, 2 colon cancer cell lines were used, namely HCT116 (a colon carcinoma cell line) and HT29 (a colon epithelial adenocarcinoma cell line). The *N*-glycome, *O*-glycome, and glycolipidome were characterized with a nanoLC–MS using a QTOF mass analyzer. The *N*- and *O*-glycome analysis employed a porous graphite carbon (PGC) stationary phase, while the glycolipidome analysis was obtained with a C18 stationary phase for chromatographic separation. The proteome and glycoproteome were determined with nanoLC-MS using a C18 column and an Orbitrap mass analyzer. We identified (including isomers) over 300 *N*-glycans, 100 *O*-glycans, and 100 glycolipids structures. In addition, nearly 1,000 proteins were identified in both cell lines from the proteomic analysis. Over 600 glycopeptides were identified from HCT116, and over 900 glycopeptides were identified from HT29 cells.

N-glycomic profile of 2D and 3D cell membrane

The *N*-glycomic profiles of the 2D and 3D cells of HCT116 and HT29 were obtained, and each yielded over 300 *N*-glycan structures (Fig. 2A and B). The 2 cell lines differ in their respective *N*-glycomic profiles as the HCT116 contained little or no fucose, so that most of the complex- and hybrid-type structures were sialylated. The lack of fucose in the glycome is due to a mutation of the GDP-Mannose 4,6-Dehydratase (GMDS) gene. This gene encodes for guanosine diphosphate (GDP)-mannose 4,6, dehydratase protein, a crucial enzyme for the synthetic pathway of fucose (Holst et al. 2016). For HT29, these structures were sialofucosylated. Large structural changes were observed that were broadly categorized by grouping them into high-mannose, undecorated (nonfucosylated nonsialylated), fucosylated (only), sialylated (only), and sialofucosylated to provide more specific comparisons of the structures. There was a 2-fold increase in high-mannose abundances in both cell lines when comparing the 3D to their 2D counterparts. Both cell lines showed statistically significant changes (based on triplicate analysis) in their *N*-glycan profile with *q*-values of no more than 0.005 based on a multi-*T*-test analysis with 1% false discovery rate (FDR) correction for each subtypes (Fig. 2C). HCT116 showed an increase from 23% (relative abundances) in the 2D model to 43% in the 3D model for high mannose structures, along with major decreases in undecorated (7%) and sialylated (12%) *N*-glycans. HT29 showed similar behavior with a 20% increase in high-mannose and a 13% reduction of sialylated *N*-glycans. In addition, HT29 showed significant increase in undecorated

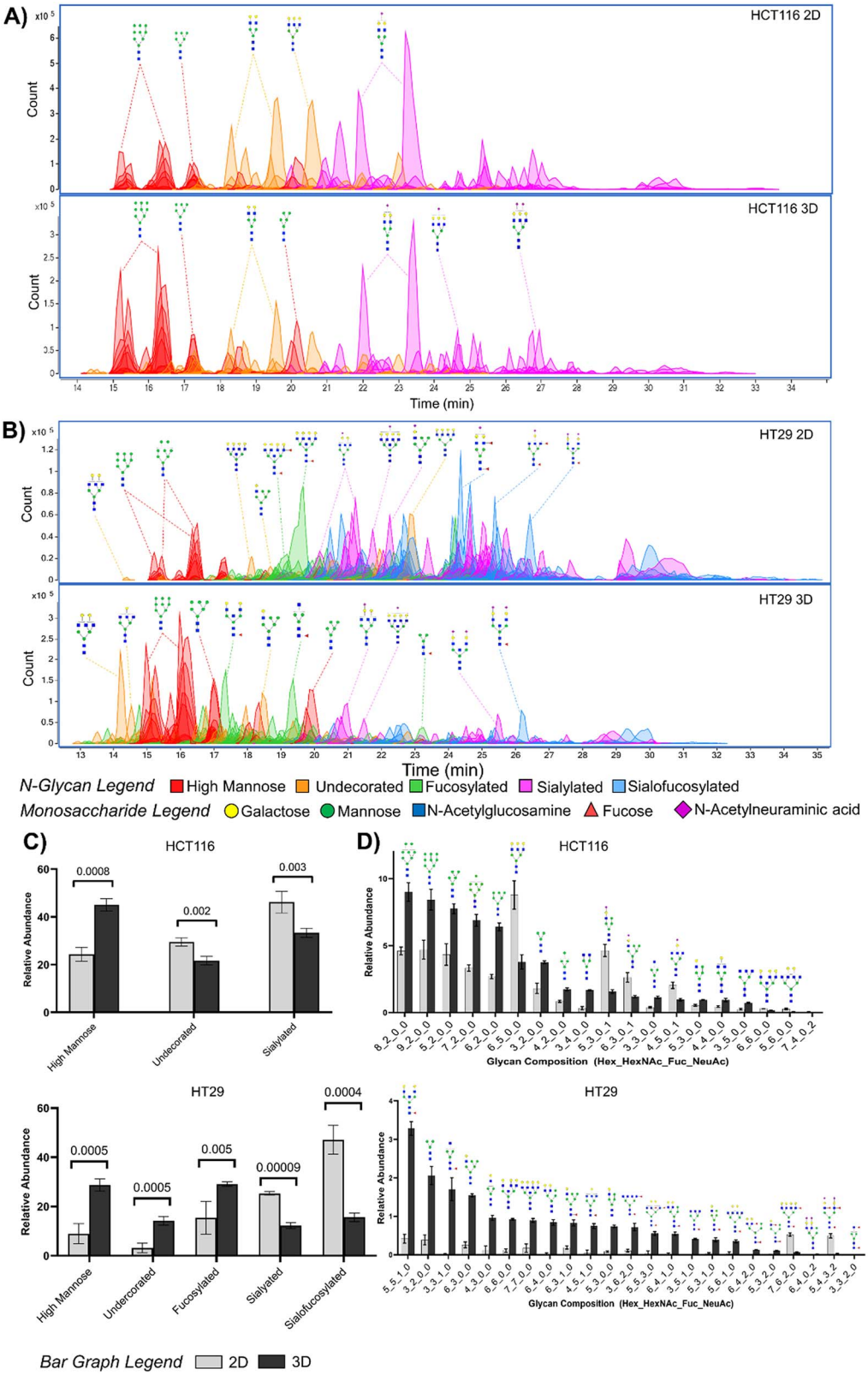

Fig. 2. Extracted compound chromatograms of the *N*-glycan for the 2D and 3D models of (A) HCT116 and (B) HT29 . The *N*-glycan structures are putative. (C) The abundances of glycan groups showed significant changes between the two models for the various glycan groups. (D) Glycoforms with the high abundances show significant changes. The peaks are colored by glycan subtypes and annotated with the schematic representation of the glycan structures. Biological replicates ($n = 3$) were prepared for all samples, and a multi-*T* test was performed with a strict 1% FDR correction.

(11%) and fucosylated (13%) *N*-glycans and decrease in sialofucosylated (31%) *N*-glycans.

The examination of individual *N*-glycan structures for HCT116 yielded 19 *N*-glycans that were found to be significantly altered in their abundances, while HT29 yielded nearly 25 altered abundances with high statistical significance (with *q*-values lower than 0.003) (Fig. 2D). With HCT116, there were 12 *N*-glycans found to be up-regulated in the 3D cells, 7 of them being high-mannose glycans. The remaining set were down-regulated in 3D cells. HT29 showed a similar trend, where 17 *N*-glycans out of the 25 *N*-glycans that were significantly increased in the 3D model. This group consisted of mainly of undecorated and fucosylated structures with only one high mannose species ($Hex_3HexNAc_2$). When a standard 2-tailed *t*-test analysis was performed for HT29, all changes to the high-mannose structures were statistically significant with *P*-values less than 0.05. In addition, the increase of fucosylated glycans was due mainly to monofucosylated glycans, with the fucose likely to be in the chitobiose core (Takahashi et al. 2009).

O-glycomic profile of 2D and 3D cell membrane

The *O*-glycans were released using reductive beta-elimination after glycolipid extraction of the membrane and complete release of the *N*-glycans. The *O*-glycan profiles yielded around 100 *O*-glycan structures (including isomers) (Fig. 3A and B). Unlike the *N*-glycan profiles, the *O*-glycan profiles showed fewer glycans and fewer changes between the 2 cell models. The differences in the chromatogram between 3D and 2D was more noticeable for HCT116 than HT29. The former had noticeably more *O*-glycan structures compared to the latter, which was dominated by a single disialylated species. Nonetheless, a consistent trend in both cell lines was an increase in sialylated *O*-glycans in the 3D model (Fig. 3C). In Figure 3D, only 2 *O*-glycans were found to be statistically significant under the previous rigorous criteria, $Hex_4HexNAc_4$ (found in HCT116) and $Hex_1HexNAc_1Fuc_1NeuAc_1$ (found in HT29). There were distinct structures that increased in both cell lines for the 3D cell, namely $Hex_2HexNAc_2NeuAc_2$, $Hex_2HexNAc_2NeuAc_1$, and $Hex_1HexNAc_1NeuAc_1$.

Glycoproteomic analysis of 2D and 3D cell membrane

Site-specific glycoproteomic analysis was performed on 2D and 3D models for both cell lines. For the data analysis, the software Byonic was used to annotate glycopeptides. The limitations of this method are known (Li et al. 2020), however, it remains the only commercial software that provides site-specific assignments of glycans. To increase the confidence of the assignments, the experimentally obtained *N*- and *O*-glycan compositions were used to annotate the glycopeptide structures. The resulting data were plotted on a volcano plot to observe changes in the glycopeptides (Fig. 4A). There were over 950 quantifiable N-glycopeptides (including glycoforms) identified in HT29 representing 170 glycoproteins. Among the glycopeptides, 250 were found to be significantly altered corresponding to 68 N-glycoproteins. HCT 116 had over 600 quantifiable N-glycopeptides (including glycoforms) corresponding to 116 N-glycoproteins. Of the glycopeptides, 135 N-glycopeptides were significantly altered representing 44 glycoproteins. The significantly altered N-glycopeptides were also aggregated into five categories: high-mannose, undecorated, fucosylated, sialylated, and sialofucosylated. The glycopeptides were plotted in a heatmap shown in Figure 4B, and the values of $\log_2$ fold changes were provided in Supplementary Tables 1 and 2.

Gene ontology and STRING network analysis were performed on the altered N-glycopeptides (Fig. 4C) to study the protein interactions and pathways affected by moving from 2D to 3D cells. Both HT29 and HCT116 have pathways associated with proteoglycans in cancer that were found to be significantly affected, including cell-adhesion molecules, focal adhesion, ECM-receptors interaction, P13K-Akt signaling, phagosome, and proteins processing in the endoplasmic reticulum. In addition, HT29 has significantly altered pathways associated with mechanisms of cancer and *N*-glycan biosynthesis.

Potential structural changes in protein associated with changes in glycosylation

Expanding on the glycoproteomics results, we studied the changes in glycan–protein interactions brought about by culturing in 3D- vis a vis 2D-cells. We surveyed the glycoproteomics results and identified glycoproteins where we obtained glycoform information on at least 50% of the putative glycosites in Uniprot (Consortium 2020). Of these glycoproteins, we focused on endoplasmin (ENPL; HSP90B1) and integrin alpha-3 (ITA3), both of which are implicated in tumorigenicity (Consortium 2020). We constructed molecular models of ENPL and ITA3 containing site-specific glycosylation data from our LC–MS/MS glycoproteomics results. For the cell line HT29, the glycoprotein ENPL with glycosites Asn217 and Asn445 was modelled with glycosite Asn217 at the interface between the dimeric ENPL proteins (Fig. 4D). Specifically, the glycosites Asn217 and Asn445 of ENPL in 2D-culture contained high-mannose *N*-glycans $Hex_6HexNAc_2$ and $Hex_3HexNAc_2$, respectively. In contrast, the respective glycosites in 3D-culture contained core-fucosylated $Hex_3HexNAc_3Fuc_1$ and tetra-antennary $Hex_7HexNAc_6$ structures. We examined the differences in interactions between the glycan and the polypeptide by enumerating the number of potential contacts (van der Waal overlap ≥ -0.4 Å) between the Asn217-glycan and amino acid residues on the polypeptide chain. Indeed, we found that the core-fucosylated $Hex_3HexNAc_3Fuc_1$ structure in 3D-culture has significantly more points of contact (74) compared to the corresponding glycan $Hex_6HexNAc_2$ structure in 2D-culture (34 interactions).

Similarly, for the cell line HCT116, we modelled ITA3 containing glycosites Asn86, Asn107, Asn265, Asn500, Asn511, Asn573, Asn605, Asn935, and Asn969. The model predicted that glycosites Asn500, Asn573, and Asn697 formed glycan-peptide contacts in ITA3 (Fig. 4D). In 2D-cultured cells, the glycosites Asn500, Asn573, and Asn697 were populated with fucosylated ($Hex_5HexNAc_6Fuc_2NeuAc_1$), high-mannose ($Hex_8HexNAc_2$), and undecorated ($Hex_6HexNAc_5$) structures, respectively. These *N*-glycans made 48, 85, and 44 glycan-protein contacts with the amino acid residues. In contrast, the 3D-cultured HCT116 glycosites Asn500, Asn573, and Asn697 contained undecorated ($Hex_5HexNAc_4$), high-mannose ($Hex_7HexNAc_2$), and undecorated ($Hex_5HexNAc_4$), respectively. The latter group of *N*-glycans produced 52, 63, and 47 glycan–peptide contacts with the ITA3 residues. Glycan–peptide contacts (van der Waal overlap ≥ -0.4 Å)

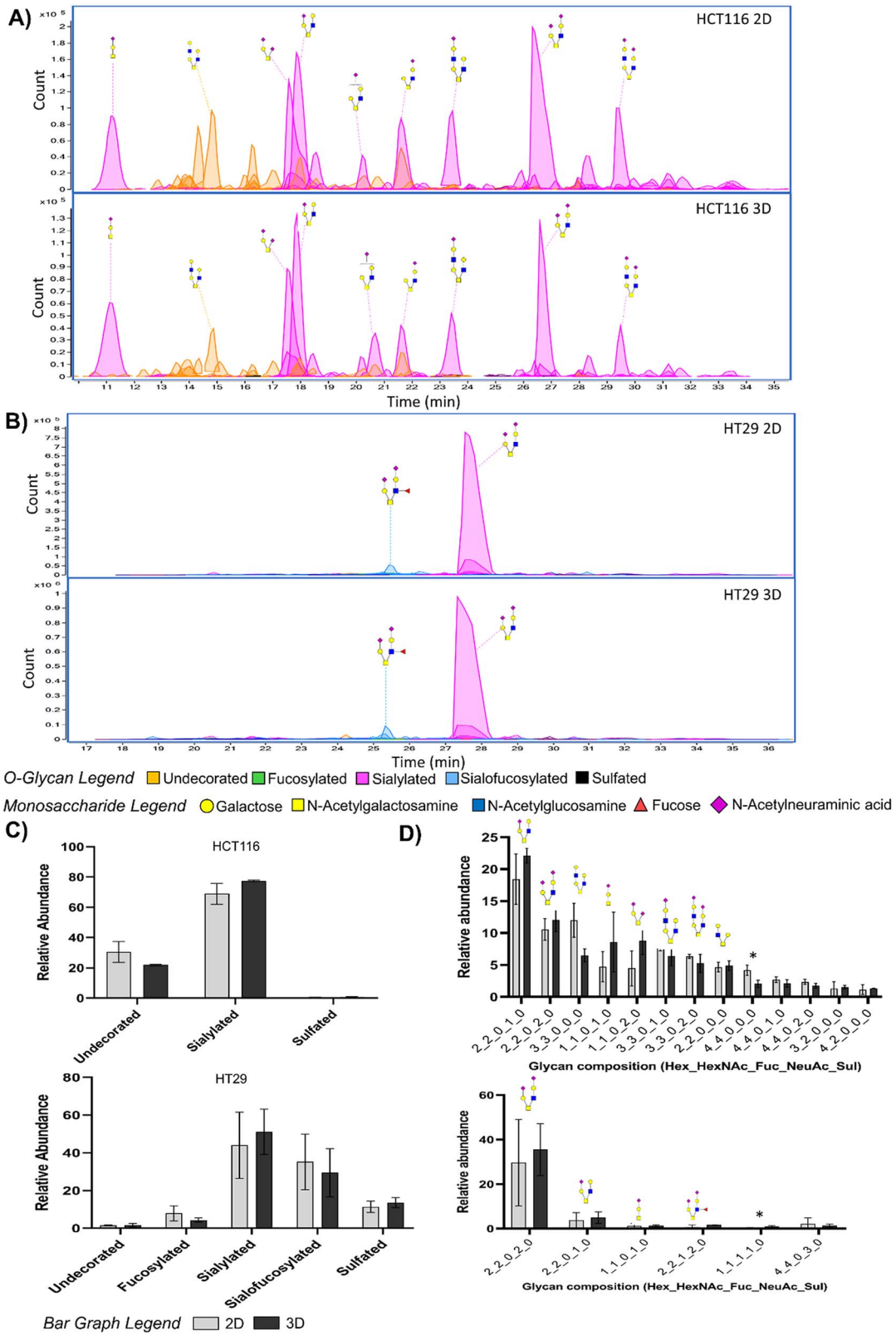

Fig. 3. Extracted compound chromatograms of *O*-glycans from the 2D and 3D models for (A) HCT116 and (B) HT29. The *O*-glycan structures are putative. (C) Quantitation of *O*-glycan groups in the two cell lines showed some variations in the glycan subtypes between the two models. (D) Individual structures show minor but statistically significant changes. Biological replicates ($n = 3$) were prepared for all samples and a 2-tailed *t*-test was performed with *P*-value <0.05 (marked by*).

of ITA3 *N*-glycans showed higher number of distinct interactions in 3D-cultured cells at glycosites Asn500 and Asn697, while higher interactions in 2D-cultured cells was predicted for glycosite Asn573. Thus it appears the 3D cells are more interactive due to glycans producing more interactions with the polypeptide chain of the same protein.

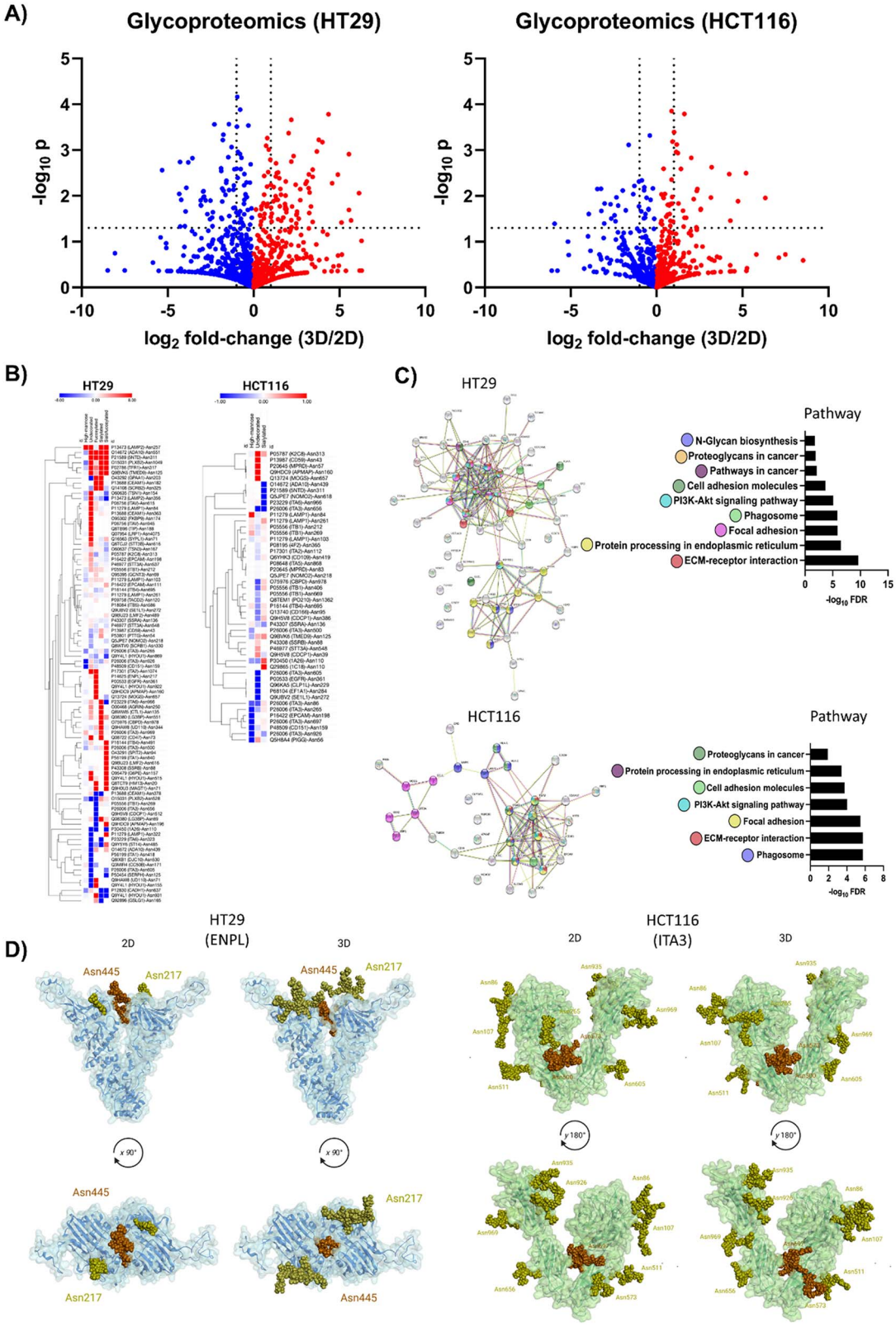

Fig. 4. Statistical analysis of the glycoproteomic results showing the glycoproteins most affected between the 2D and 3D model. (A) Volcano plot for HT29 and HCT116. (B) Heatmap of significant glycopeptides. (C) The gene ontology and STRING network analysis of significant glycopeptides. (D) Glycoproteomic simulation of ENPL and ITA3. Biological replicates ($n = 3$) were prepared for all samples and a multi-T test was performed with 1% FDR correction.

From the modeling experiments, we found differences in protein glycosylation that affect the physical interactions of the glycans with amino acid residues in the protein complex.

Spatial variations in the *N*-glycomic profile of 3D cell

To further study the variations in glycosylation between the cell models, an enzymatic peeling of the spheroid was performed with Accutase. The peeling assay separated the spheroids into 3 components, the outer layer (proliferation layer), the middle layer (quiescent layer), and the inner layer (necrotic core) (Liu and Hummon 2015). An apoptosis assay was performed on the 3 layers isolated from the peeling assay for both cell lines (Fig. 5C and D). The final fraction (the necrotic core) in both cell lines showed a significant fraction of dead cells compared to the proliferation and quiescent layer, especially for HT29 spheroids where the percentage of live cells dropped from the 96% to less than 60%. A video of the peeling process with Accutase and HCT116 was provided (Supplementary Video 1). The enzymatic peeling of HCT116 released the cells but did not disrupt the 3D spheroid structure.

The *N*-glycomic profile of each layer was determined for both cell lines, and each yielded at least 150 *N*-glycans (including isomers) (Fig. 5A and B). The high-mannose type glycans were the most abundant in the proliferation layer (41% in HCT116 and 32% in HT29) of both cell lines. Additionally, the necrotic core yielded more *N*-glycans than the proliferation layer and was composed of more complex-type structures. The relative abundances of each *N*-glycan was plotted for both cell lines in Supplementary Figures 1 and 2. The other glycomic analyses were not performed on the 3 fractions due to limited samples from the enzymatic peeling.

Glycolipidomic profile of 2D and 3D cell membrane

The glycolipids were isolated using Folch extraction of the sample after *N*-glycan release. The isolated glycolipids were characterized by LC–MS for both cell lines, and each yielded over 100 distinct glycolipids (including isomers) (Fig. 6A and B). Both cell lines showed a similar trends with increasing sialylated glycans in 3D models compared to 2D models (5% increase in HCT116 and 25% in HT29). Additionally, 2D models seemed to express more undecorated and sulfated glycans and increase in global (1%) glycans in 3D models in HCT116 (Fig. 6C). In HT29, there were more fucosylated glycolipids in the 2D cells. These alterations were found to be statistically significant with q values of 0.0003 or less. With the ceramide backbone, the HCT116 model showed more diversity compared to HT29 (Fig. 6D). In HCT116, the significant ceramide backbones were d32, d36, d38, d40, and d44, with a q value of 0.001 or less. In addition, HT29 decreased relative abundances of t34 and t42 ceramide (which was not found in HCT116) and increased d40 and d42 ceramide in the spheroid model. Both cell lines showed consistency of having d34 as the most abundant ceramide and showed a slight elevation in d34 and d32 in the 3D models (though the alteration was not significant). For the individual glycolipids, 34 glycolipids (including isomer) in HCT116 and 73 glycolipids (including isomer) in HT29 were found to be significant with a 1% FDR correction. Among these, following glycolipids were found in both models, namely Hex_2NeuAc_1-d34_1, $Hex_3HexNAc_1NueGc_2$-d42_1, $Hex_3HexNAc_1NeuAc_1$-d34_1, $Hex_2HexNAc_1$-d34_1, $Hex_3HexNAc_1$-d34_1, $Hex_3HexNAc_1NeuAc_2$-d42_1, $Hex_2HexNAc_1NueGc_1$-d34_1, Hex_2-d34_1, Hex_3-d34_1, $Hex_4HexNAc_2$-d34_1, $Hex_3HexNAc_3NeuAc_1$-d40_1. In HT29, one of the largest altered glycolipid abundance was for Hex_4NeuAc_3-d34_1 with a $\log_2$ fold change of 6.1 and a q-value of 0.003.

Proteomic analysis of 2D and 3D cell membrane

Proteomic analysis was performed separate from the glycoproteomic analysis on the enriched membrane fractions of the 2D and 3D models. As with the *N*-glycans, the proteomic analysis showed dramatic changes in both cell lines. The volcano plot of the proteomic data for HT29 yielded over 1,200 reproducibly quantifiable proteins with almost 50% significantly altered (Fig. 7A). HCT116 had over 900 proteins, and over 30% of the proteins were significantly altered. The proteomic results for HT29 was comparable to a previous study of whole-cell proteomic analysis of HT29 comparing 2D and 3D cultures (Yue et al. 2016). There were many upregulated proteins responsible for programmed cell death found in HT29 (Supplementary Fig. 3A). HCT116 had proteins related to cell death, but not as many as HT29 (Supplementary Fig. 3B). Other biological functions altered between the 2D and 3D models were adhesion, cellular response, and N-glycosylation. Both HT29 and HCT116 had significantly altered proteins in biological processes related to central carbon metabolism in cancer (Supplementary Fig. 3C). In addition, HT29 had significantly up-regulated proteins essential in colorectal cancer (Supplementary Fig. 3D). Gene ontology analyses were performed using the proteins that were significant altered. In HT29, 340 pathways were up-regulated, and 338 pathways were down-regulated. HCT116 had less, 26 were up-regulated, and 113 were down-regulated (Supplementary Fig. 4).

To further examine the proteomic results, we performed a comparative analysis both cell lines with the different culturing method. PCA analysis of the data showed that each cell line and its culturing methods were tightly clustered, forming 4 distinct clusters (Fig. 7B). Additionally, a heat map was generated with the abundances (Fig. 7C). Most of the protein expressions were unique except for one section where there was a consistent trend of down-regulated proteins in the 2D models and up-regulated proteins in the 3D models regardless of the cell line. The affected pathway was plotted, displaying the up-regulated or down-regulated pathways based on the proteins' expression level (Fig. 7D). A few pathways were up-regulated in the 3D models that correspond to carbohydrate regulation, namely glucose metabolism, gluconeogenesis, metabolism of carbohydrates, and glycolysis. In addition, some pathways were found to be consistently down-regulated in both 3D models, namely stabilization of p53 and DNA damage checkpoint.

Discussion

The *N*-glycomic, *O*-glycomic, glycolipidoimic, proteomic, and glycoproteomic profiles were obtained to provide the most extensive characterization of the 2D and 3D cultured cells of 2 types of colon cancer cells (HCT116 and HT29). HCT116 (a microsatellite instability human colorectal carcinoma with a KRAS mutation) and HT29 (a microsatellite stable human colorectal adenocarcinoma with a P53 mutation) represent some of the most common types of mutation found in

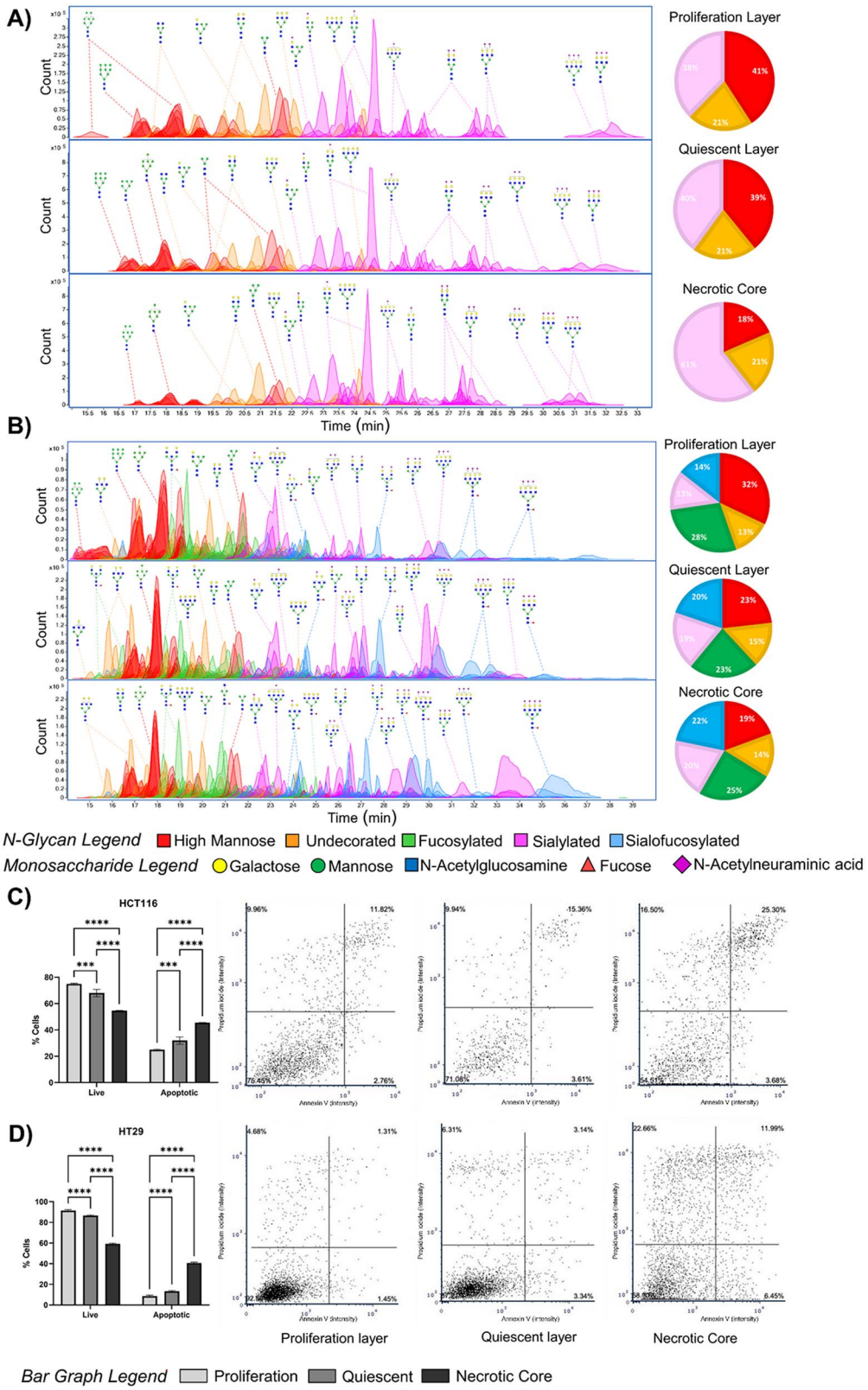

Fig. 5. Extracted compound chromatograms of the spatial profile of *N*-glycans for (A) HCT116 and (B) HT29. The *N*-glycan structures are putative. Apoptosis assay of (C) HCT116 and (D) HT29 with the significant change in dead cells. The peaks are colored by glycan subtypes and annotated with the schematic representations of the glycan structures. Biological replicates ($n = 3$) were prepared for apoptosis assay and 2-tailed *t*-test was performed with *P*-value <0.05 is *, <0.01 is **, <0.001 is ***, and <0.0001 is ****.

colorectal cancer (Yao et al. 2005; Duldulao et al. 2012). The multi-glycomic results showed dramatic alteration in both cell lines when comparing the 2D and 3D models. They showed upregulation in cancer-related glycans, proteins, and glycoproteins providing further evidence that the 3D model is closer to the disease than the standard 2D.

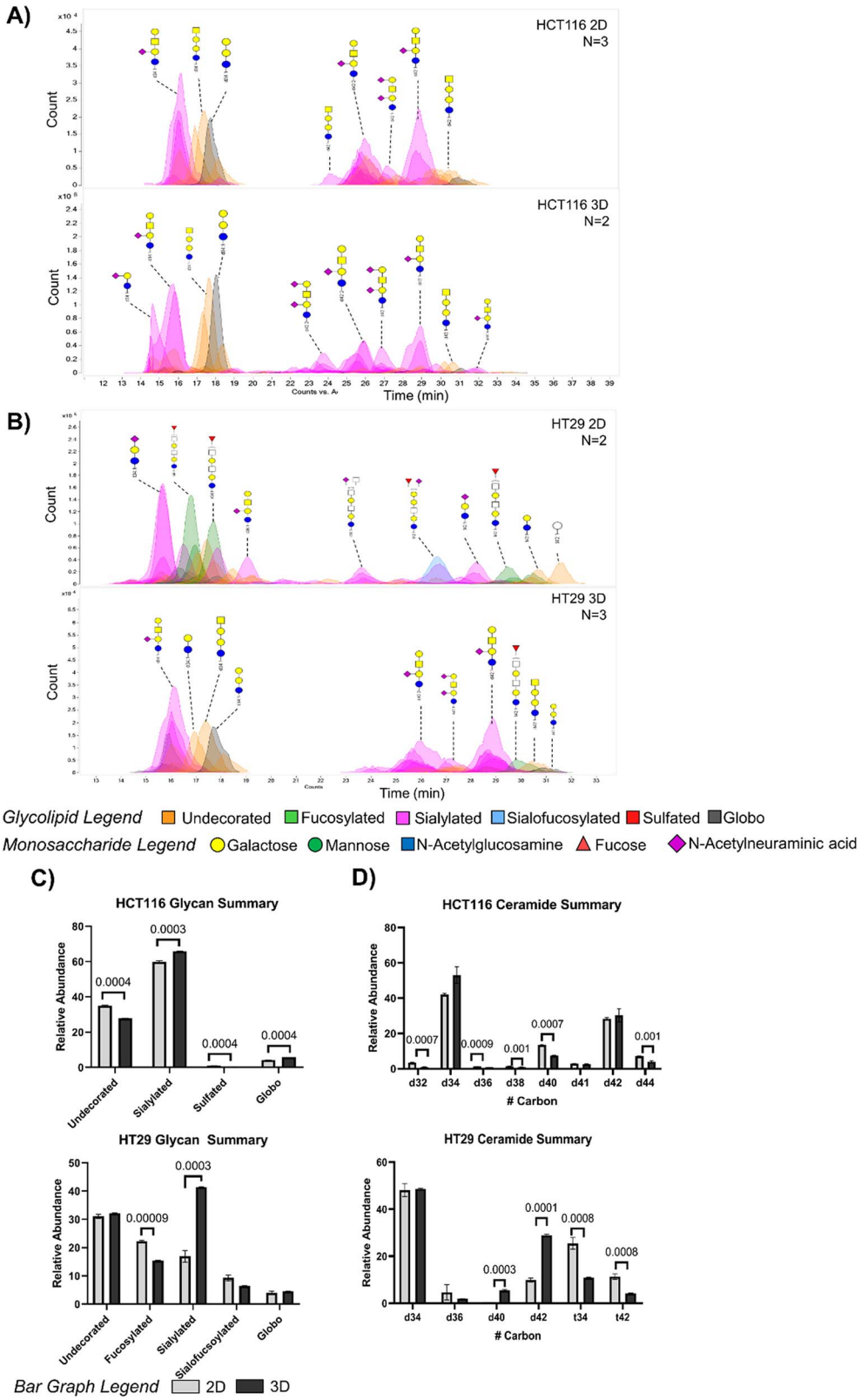

Fig. 6. Extracted compound chromatograms of the glycolipid profile of the 2D and 3D models for (A) HCT116 and (B) HT29. The glycolipid structures are putative. (C) The significant glycan for HCT116 and HT29 with their *q* values. (D) The significant ceramides for HCT116 and HT29 with their *q* values. The peaks are colored by glycan subtypes and annotated with the schematic representation of the glycan structures. Multi-*T* test was performed with 1% FDR correction.

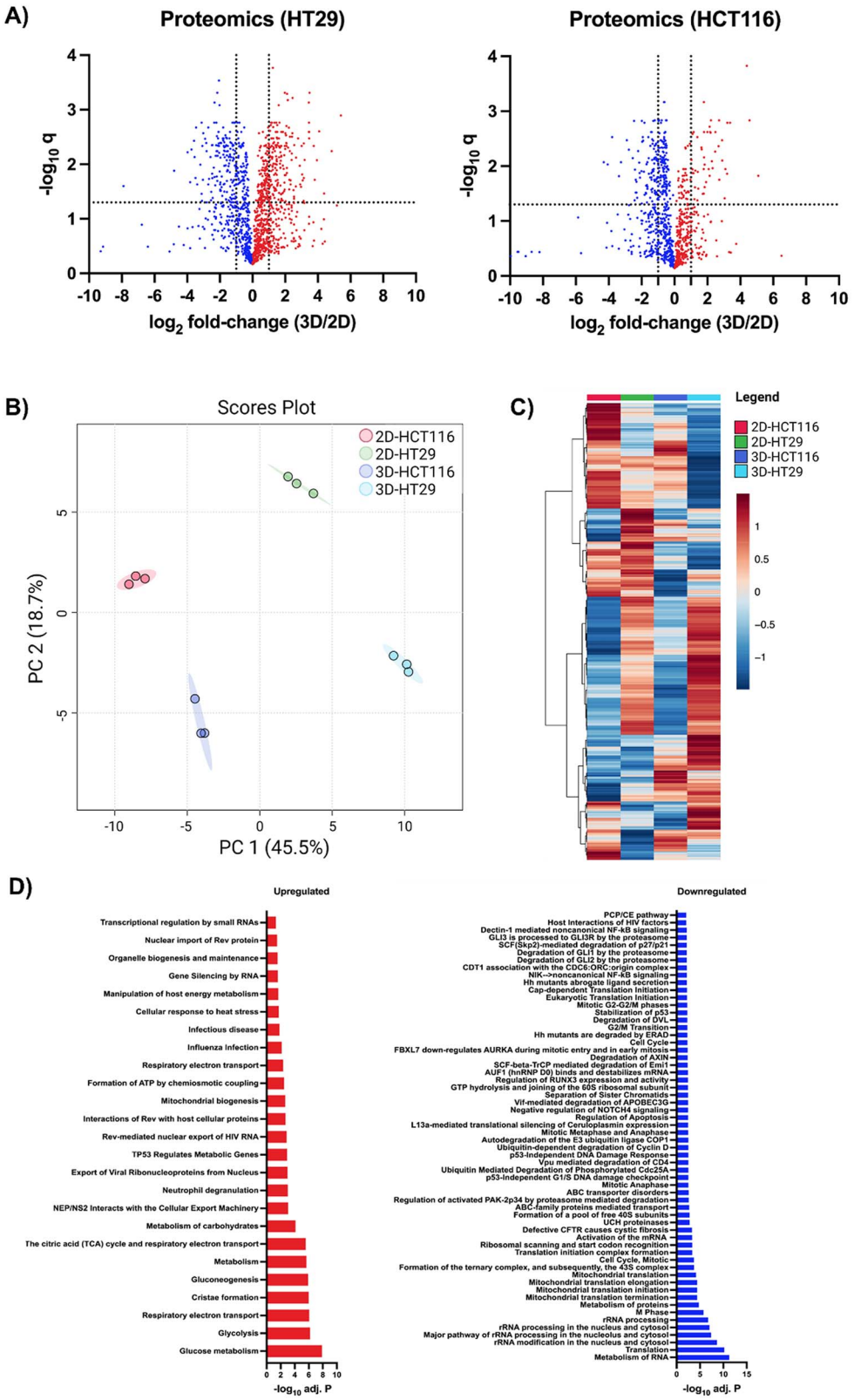

Fig. 7. Proteomic results of the 2D and 3D model. (A) The volcano plot of HT29 and HCT116 and (B) PCA plot of the 2D and 3D model of both HT29 and HCT116 cell line. (C) Heatmap of the 2D and 3D model of both cell line HT29 and HCT116. (D) The up- and down-regulated pathways that were with the 2D model of HCT116 and HT29 and 3D model. Biological replicates ($n = 3$) were prepared for all samples and a multi-T test was performed with 1% FDR correction.

Increases in fucosylated and sialylated glycans for colorectal cancer compared to the non-cancerous cells have been previously reported (Holst et al. 2016). Indeed, the 3D model of HT29 showed increase in fucosylated glycans (mainly singly fucosylated) compared to the 2D. Fucosylated glycans were not expected and not found in HCT116. With sialylation, the *N*-glycan profile showed a decrease in sialylated glycans, however, the decrease was compensated by the glycolipid profile which showed increased sialylation for both HCT116 and HT29 cell lines. Previous studies have also shown increases in glycolipid sialylation in the cancer tissues compared to the non-cancer (Taki et al. 1988). Interestingly, both cell lines also showed consistent increases in high-mannose type *N*-glycans, which play essential role in the metastatic characteristics of cancer cells. Increases in high-mannose glycans in breast cancer cell lines made the cells more metastatic by increasing cell migration and cell proliferation rates (de Leoz et al. 2011; Park et al. 2020; Oh et al. 2021). There have also been suggestions that *O*-glycans increase in colon cancer (Yang et al. 1994; Brockhausen 2006), however, there was little or no increase between 2D and 3D.

This *N*-glycome varied between the different layers of the spheroid with consistent behavior among the 2 cell lines. The spheroids' most outer layer, the proliferation layer, expressed the highest relative abundance of high-mannose glycans in both cell lines. Deeper in the spheroid, into the non-proliferating layers, the *N*-glycan compositions became more structurally diverse with increasing abundances of complex-type structures. Cell proliferation may indeed require more high-mannose type *N*-glycans. Proliferation is associated with higher protein turnover and high-mannose glycans have been shown to increase protein turnover compared to complex-type (Wong, Xu, Barboza, et al. 2020a).

Analysis of the significantly altered glycopeptides in HT29 and HCT116 provided indications of the large glycoproteomic changes in the cell glycocalyx between the 2D and 3D models. The glycoproteins affected were mainly integrin proteins (ITGAV, ITGA3, ITGA2, ITGB1, ITGA6) and EGFR. For example, ITGB1 at site Asn212 showed increases in undecorated, fucosylated, sialylated, and sialofucosylated glycans in the HT29 cell model. With EGFR, there was an 8-fold increase in fucosylated glycans at Asn361. However, the proteomic analysis of these 2 proteins did not show a significant change in the protein expression, indicating the effects are most generally glycosylation-dependent. Another interesting glycoprotein found in HT29 was carcinoembryonic antigen (CEA), a glycoprotein associated with colorectal cancer. The results here match a previous study that showed an increase in fucosylated glycans in tumor-associated CEA (Chandler et al. 2016; Zhao et al. 2018). In the 3D model of HT29, the fucosylated glycopeptide of CEA at Asn363 (Hex6HexNAc6Fuc2) had a $\log_2$-fold change of 5.5 with a $-\log_{10}$ *P*-value of 4. Homology modeling added additional insight into the changes induced by varying glycan structures. By using the site-specific glycoprotein information for selected glycoproteins (ENPL and ITA3), increased interacts were observed due primarily to increased hydrogen bonding in the 3D cells compared to the 2D.

Comparison of the 2D and 3D proteomic results also showed dramatic biological changes, including the increases in cell death and apoptosis pathways. These results are likely due to the formation of a necrotic core in the 3D model. In addition, both cell lines displayed an upregulation of Lactate dehydrogenase A (LDHA) and KPYM, which are responsible for central carbon metabolism in cancer (Hsu and Hung 2018; Zhu et al. 2018). HT29 also had a significant alteration with 8 proteins (MP2K1, RHOA, RALB, RAC1, CTNB1, KRAS, CYC, and RALA) that were directly correlated to colorectal cancer. These results provide further indications that the 3D model is more cancer-like and associated with increases in cell-to-cell interactions producing microenvironments similar to conditions found in tumors.

Conclusion

Spheroids of cells as 3D models for tumors are more attractive than the traditional 2D cultures as they better represent the physiological conditions in diseases. Deep structural analysis of the glycocalyx now provides molecular reasons for why the model is more accurate. Multi-glycomic analysis suggests greater degrees of molecular interactions in the spheroid model thereby accompanying greater physical interactions between cells. These interactions are strongly affected by the glycan structure and the differences between the 2D and 3D models with regard to the *N*-glycome, *O*-glycome and the respective glycoproteome and glycolipidome. In turn, these interactions affect greatly the biology by altering the interactions of oncoproteins and cancer-related pathways.

This work further represents the need and utility of the multi-glycomic workflow for understanding the role of glycosylation in diseases such as cancer. As glycan-specific therapeutics emerges, these studies could also provide new targets for therapeutics and diagnostics.

Materials and methods

HCT116 and HT29 cell lines, and McCoy's 5A medium, were obtained from the American Type Culture Collection (ATCC). Dithiothreitol (DTT), iodoacetamide (IAA), and ultra-low attachment 96 well plates were purchased from Sigma-Aldrich. Phosphate Buffered Saline (PBS), fetal bovine serum (FBS), penicillin, and Accutase were purchased from ThermoFisher Scientific. Sequencing grade trypsin and Glu-C were purchased from Promega. ISPE-HILIC cartridges were purchased from HILICON AB (Sweden).

Cell line culture

Human colon adenocarcinoma epithelial HT29 cells and human colon carcinoma epithelial HCT116 cells were obtained from ATCC and grown in McCoy's 5A medium supplemented with 10% (v/v) FBS, and 1% (v/v) penicillin incubated at 37 °C in an atmosphere of 5% CO_2. Half volume media changes were done every 48 h for 14 days. Ultra-low attachment 96 well plates (Sigma-Aldrich) were used for spheroid culture. Each well was seeded with 5,000 cells supplemented with 150 μL of media.

Enzymatic accutase peeling of spheroids

Cells from spheroids were fractionated into 3 distinct physiological populations using accutase (Thermo Fisher Scientific) treatment. Accutase was warmed to 37 °C before treatment. Spheroids were washed twice with PBS to remove any media in the cell culture dish, followed by the addition of 2 mL of accutase. The cells were incubated at 37 °C and shaken at 70 rpm for 5 min. The detached cells in accutase were collected (proliferation layer), then washed again with 2 mL of PBS. The

process was repeated once more to collect the hypoxia layer. The remaining cells were collected and labeled as the necrotic core. The 3 fractions were subjugated to centrifugation and stored in Hepes buffer at −80 °C until prepared for cell membrane extraction. Ninety-six spheroids were used for the *N*-glycomic analysis.

Cell-membrane extraction

Extraction protocols were described previously and applied here with slight modifications (Park et al. 2018). Briefly, cellular debris and mitochondrial fractions were pelleted by centrifugation at 2,000 × *g* for 10 min. Supernatants were transferred to perform ultracentrifugation at 200,000 × *g* for 45 min at 4 °C. Pelleted plasma membrane was then resuspended in 500 μL of 0.2 M Na_2CO_3 and 500 μL of nanopure water followed by 2 series of ultracentrifugation at 200,000 × *g* for 45 min to wash off cytoplasmic and endoplasmic reticulum fractions.

Protein digestion

Digestion protocols were described previously and applied here with slight modifications (Li et al. 2019). The cell pellet was sonicated with 60 μL of 8 M urea for 20 min followed by the addition of 2 μL of 550 mM DTT incubated at 55 °C for 50 min. After incubation, 4 μL of 450 mM of IAA was added and placed in the dark for 20 min. Then, 420 μL of 50 mM ammonium bicarbonate (ABC) was added, followed by 2 μg of trypsin (reconstituted in 50 mM ABC). An additional 2 μg Glu-C (reconstituted in 50 mM ABC) was added for the glycoproteomic sample. All samples were then incubated at 37 °C for 18 h. For proteomic analysis, peptides were desalted using C18 cartridges SPE. For glycoproteomic analysis, the samples were dried and desalted using HILIC cartridges SPE. The peptide and glycopeptide concentrations were determined with bicinchoninic acid assay (BCA) peptide assay (ThermoFisher Scientific) prior to injection in the Orbitrap Fusion Lumos nanoLC–MS/MS instrument.

Extraction of the glycocalyx

Glycocalyx extractions were described previously and applied here with slight modifications (Li et al. 2020). After cell-membrane extraction, the membrane pellet was reconstituted in 100 μL of 100 mM ABC and 5 mM DTT. Each sample was heated at 100 °C for 1 min to denature proteins. An aliquot of 2 μL of 500,000 U/mL peptide N-glycosidase F (PNGase F) was added to each sample and microwaved at 60 °C for 10 min to accelerate *N*-glycans release. Afterward, the samples were incubated for 18 h at 37 °C to hydrolyze the *N*-glycans. The reaction was quenched with 350 μL of water and subjected to ultracentrifugation at 200,000 × *g*. The supernatant was extracted and cleaned with PGC solid phase extraction (SPE) and dried. The remaining pellet was dried under vacuum for 10 min, followed by Folch or Bligh–Dyer extraction to separate the glycolipids. The supernatant was extracted after centrifugation at 8,800*g* for 5 min at 25 °C. The addition of 100 μL of 0.1 M potassium chloride was added to the supernatant and centrifuged for 8,800*g* for 5 min at 25 °C. The aqueous layer was extracted, dried, washed with C8 SPE plate, and dried again. The remaining pellet was dried again under vacuum, then rehydrated with 90 μL of water and sonication for 20 min. *O*-glycans were chemically released using B-elimination and were performed by adding 100 μL of 2 M $NaBH_4$ and 10 μL of 2 M NaOH. Samples were incubated at 45 °C for 18 h. Samples were cleaned with PGC SPE, dried, HILIC SPE, and dried again. *N*-glycans and *O*-glycans were reconstituted in water, and glycolipids were reconstituted in 1:1 (vol/vol) methanol/water before NanoLC-chip-Q-TOF MS Analysis.

N- and *O*-glycan and glycolipid analysis with nanoLC chip-QTOF

The glycocalyx analysis was described previously and applied here with slight modifications (Ozcan et al. 2013; Li et al. 2020; Wong, Xu, Park, et al. 2020b). The *N*-glycans, the *O*-glycans, the glycolipids were separated using a nanoLC Chip–QTOF MS with a 65 min gradient, where the glycans begin to elute between 10 and 40 min. *N*-glycans, *O*-glycans, and glycolipids separation was conducted with a binary solvent system. Solvent A composed of 3% (v/v) acetonitrile (ACN) and 0.1% (v/v) formic acid (FA) in water, and solvent B composed of 90% (v/v) ACN and 1% (v/v) FA in water for *N*- and *O*-glycans separation. Solvent A composed 20 mM ammonium acetate and 0.1% acetic acid in water, and solvent B composed 20 mM ammonium acetate and 0.1% acetic acid in 85:15 (v/v) methanol/isopropanol for glycolipid separation. The *N*- and *O*-glycans were injected into an Agilent PGC microfluidic chip consisting of a 40 nL enrichment and a 43 mm × 75 μm analytical column, with a particle size of 5 μm. The gradient sequence for the *N*- and *O*-glycans analysis was: 0–2.5 min, 1% B; 2.5–20 min, 16% B; 20–35 min, 58% B; 35–40 min, 100% B; 40–50 min, 100% B; 50.01–65 min, 0% B with a flow rate of 0.3 μL/min. The glycolipids were injected into an Agilent C18 microfluidic chip consisting of a 40 nL enrichment and a 150 mm × 75 μm analytical column, with a particle size of 5 μm. The gradient sequence for the glycolipid analysis was: 0–1 min, 70% B; 1–4 min, 85% B; 4–40 min, 100% B; 40–55 min, 100% B; 55–58.1 min, 70% B; 58.1–65 min, 70% B with a flow rate of 0.3 μL/min. The *N*-glycans, *O*-glycans, and glycolipids analysis mass range was *m/z* 600–2,000, *m/z* 400–2,000, and *m/z* 500–2,000, respectively, with spectra measured at 0.8 s per spectrum in positive mode ionization. Reference mass *m/z* 1221.991 was used to correct mass inaccuracies. The cell-surface glycosylation changes were quantified using MassHunter software (Agilent, Santa Clara, CA, USA, version B.07.00).

Proteomic analysis with nanoLC–MS/MS

Proteomic analysis of peptides was separated onto a C18 column, 150 mm × 75 μm with a particle size of 2 μm 100 Å, at a flow rate of 0.3 μL/min with a binary solvent system with solvent A containing 0.08% (v/v) formic acid (FA) in water and solvent B containing 80% ACN (v/v) 0.1% (v/v) FA in water. Solvent gradient for peptide separation was: 0 min 4% B; 0–3 min, 9% B; 3–6 min, 12% B; 6–80 min, 24% B; 80–95 min, 50% B; 95–99 min, 99% B; 99–103 min, 99% B; 103–103.5 2% B 103.5–120 min 2% B. Mass range of *m/z* 375–1,500 for MS1 and mass range of MS2 was set to auto. Raw output files were then inputted into Byonic software for peptide analysis, followed by an extracted ion chromatogram (EIC) using Byologic software (Protein Metrics).

Glycoproteomic analysis with nanoLC–MS/MS

Glycoproteomic analysis was described previously and applied here with slight modifications (Li et al. 2020).

Glycopeptides were separated onto a C18 column, 150 mm × 75 μm with particle size of 2 μm 100 Å, at a flow rate of 0.3 μL/min with a binary solvent system with solvent A containing 0.08% (v/v) FA in water and solvent B containing 80% ACN (v/v) 0.1% (v/v) FA in water. Mass range of *m/z* 700–2,000 for MS1 and mass range of MS2 was *m/z* 120 and greater. Raw output files were then inputted into Byonic and Byologic software for glycopeptide analysis (Protein Metrics).

Apoptosis assay

Three-dimensional spheroids of HCT116 and HT29 cells were cultured at 37 °C, 5% CO_2 for 14 days. First, spheroids were collected from ultralow-attachment plates by pipetting, and then the proliferation, hypoxia, and necrotic core layers were separated using Accutase treatment. The apoptosis assay was performed using Nexcelom Annexin V-FITC/PI™ Apoptosis kit according to manufacturer instructions. After harvesting the cells via trypsinization, aliquots were prepared to contain approximately 600,000 cells for each sample. The cell suspensions were subsequently centrifuged at 400*g* for 5 min and then resuspended in 40 μL Annexin V binding buffer, making sure to resuspend the cells completely. Then, 5 μL each of Annexin V-FITC and PI stains were added to the cell suspensions. These were incubated for 15 min at 37 °C in the dark. After incubation, 250 μL of PBS was added to each sample and then centrifuged at 400*g* for 5 min, carefully removing the supernatant. The cells were finally resuspended in 100 μL Annexin V binding buffer before data acquisition. Data was acquired using Cellometer Vision CBA 5, using the protocol CBA_Annexin V + PI assay, with an F1 exposure time of 8,000 ms and F2 exposure time of 20,000 ms. Acquired data were analyzed using FCS Express 7.0. Cell gating was adjusted using the proliferation layer cells as control. Assays were done in triplicate.

Quantitative analysis of proteomic and glycoproteomic data

The mass spectrometry data were analyzed using the Byos workflow (Protein Metrics). For qualitative analysis in Byonic (Protein Metrics), proteins were compared to the human proteome database using a precursor mass tolerance of 20 ppm and fragment mass tolerance of 10 ppm[26] (Consortium 2020). The digestion parameters used included C-terminal cleavage by trypsin (K and R cleavage sites) with at most two missed cleavages. The following peptide modifications were included: carbamidomethyl @ C, oxidation @ M, deamidation @ N and Q, acetylation at protein *N*-terminal, Gln to pyro-Glu at *N*-terminal Q, Glu to pyro-Glu at *N*-terminal E. Protein IDs were filtered at 1% FDR. To identify the glycoproteins and glycoforms, an additional search was performed in Byonic using an in-house *N*-glycan database. Quantification for each protein was done in Byologic (Protein Metrics) by quantifying the XIC area sum of the top 3 most abundant peptides. XICs were then normalized to sum total before statistical analysis. On the other hand, glycoform quantification was normalized to each protein's glycosite to yield the percentage occupancy of a particular glycoform.

Gene ontology analysis of proteomic and glycoproteomic results

To identify significantly different proteins and glycopeptides, multiple *t*-tests were conducted in GraphPad Prism using an FDR approach (FDR = 5%). Significantly over- and under-expressed proteins were annotated using g:profiler software and STRING (Szklarczyk et al. 2018; Raudvere et al. 2019). Comparative protein expression between 2D- and 3D-cultured HT29 and HCT116 cells were mapped out using Metaboanalyst software (Pang et al. 2021). Similarly, the glycopeptides were annotated using STRING to yield significantly enriched KEGG pathways. Significantly different glycopeptides were plotted as a heatmap in Morpheus (Broad Institute (n.d.). Morpheus. https://software.broadinstitute.org/morpheus/).

Glycoproteomic profiling of ENPL and ITGA6

Based on the glycoproteomics analysis, ENPL (P14625) and ITGA3 (P26006) were identified as potentially significant glycoproteins in HT29 and HCT116, respectively. The glycoforms quantified from these proteins were extracted and compared between 2D- and 3D-cultured cells. The glycoforms that had the greatest difference in abundance were selected to be modelled into ENPL and ITGA3. Protein structures of ENPL and ITGA3 were homology modelled using SWISS-MODELLER (https://swissmodel.expasy.org/) (Waterhouse et al. 2018) using GRP94 (PDB ID: 2o1u) and ITGAV (PDB ID: 3ije) as templates for ENPL and ITGA3, respectively. PDB files of these homology models were subsequently glycosylated at specific asparagine residues (obtained from glycoproteomics result) using Glycan-modeller in CHARMM-GUI (https://charmm-gui.org/?doc=input/glycan) (Park et al. 2019). The modelled fully-glycosylated ENPL and ITGA3 were then assessed for glycan-protein using the "Find clashes/contacts" tool in Chimera, which considers atoms that have a VDW overlap ≥−0.4 Å (Pettersen et al. 2004).

Supplementary data

Supplementary material is available at *Glycobiology* Journal online.

Funding

Research was supported by the Institute of General Medicine in the National Institutes of Health (RO1 GM049077). The content is solely the responsibility of the authors and does not necessarily represent the official views of the National Institutes of Health.

Conflict of interest statement

None declared.

Data availability

NA.

Authors' contributions

Designed the study: C.B.L., R.C.N.
Supervised the study: C.B.L., R.C.N., A.B.H.
Performed experiments: Q.Z., K.S., J.T., L.M.S., M.L., C.N.
Performed statistical analysis: Q.Z., M.R.A., K.S., J.T.
Analyzed data: Q.Z., M.R.A., K.S., J.T., M.L., C.N.
Interpret data: Q.Z., C.B.L., A.B.H., F.T.
Wrote the manuscript: Q.Z., C.B.L.

References

Brockhausen I. Mucin-type *O*-glycans in human colon and breast cancer: glycodynamics and functions. *EMBO Rep*. 2006:**7**(6):599–604.

Caragher S, Chalmers AJ, Gomez-Roman N. Glioblastoma's next top model: novel culture systems for brain cancer radiotherapy research. *Cancers (Basel)*. 2019:**11**(1).

Chandler PD, Akinkuolie AO, Tobias DK, Lawler PR, Li C, Moorthy MV, Wang L, Duprez DA, Jacobs DR, Glynn RJ et al. Association of N-linked glycoprotein acetyls and colorectal cancer incidence and mortality. *PLoS One*. 2016:**11**(11):e0165615.

Consortium TU. UniProt: the universal protein knowledgebase in 2021. *Nucleic Acids Res*. 2020:**49**:D480–D489.

Daniotti JL, Vilcaes AA, Torres Demichelis V, Ruggiero FM, Rodriguez-Walker M. Glycosylation of glycolipids in cancer: basis for development of novel therapeutic approaches. *Front Oncol*. 2013:**3**: 306.

Duldulao MP, Lee W, Le M, Chen Z, Li W, Wang J, Gao H, Li H, Kim J, Garcia-Aguilar J. Gene expression variations in microsatellite stable and unstable colon cancer cells. *J Surg Res*. 2012:**174**(1):1–6.

Holst S, Deuss AJ, van Pelt GW, van Vliet SJ, Garcia-Vallejo JJ, Koeleman CA, Deelder AM, Mesker WE, Tollenaar RA, Rombouts Y et al. N-glycosylation profiling of colorectal cancer cell lines reveals Association of Fucosylation with differentiation and caudal type Homebox 1 (CDX1)/villin mRNA expression. *Mol Cell Proteomics*. 2016:**15**(1):124–140.

Hsu M-C, Hung W-C. Pyruvate kinase M2 fuels multiple aspects of cancer cells: from cellular metabolism, transcriptional regulation to extracellular signaling. *Mol Cancer*. 2018:**17**(1):35.

Kailemia MJ, Xu G, Wong M, Li Q, Goonatilleke E, Leon F, Lebrilla CB. Recent advances in the mass spectrometry methods for glycomics and cancer. *Anal Chem*. 2018:**90**(1):208–224.

Katt ME, Placone AL, Wong AD, Xu ZS, Searson PC. In vitro tumor models: advantages, disadvantages, variables, and selecting the right platform. *Front Bioeng Biotechnol*. 2016:**4**:12.

de Leoz ML, Young LJ, An HJ, Kronewitter SR, Kim J, Miyamoto S, Borowsky AD, Chew HK, Lebrilla CB. High-mannose glycans are elevated during breast cancer progression. *Mol Cell Proteomics*. 2011:**10**(1):M110.002717.

Li Q, Xie Y, Xu G, Lebrilla CB. Identification of potential sialic acid binding proteins on cell membranes by proximity chemical labeling. *Chem Sci*. 2019:**10**(24):6199–6209.

Li Q, Xie Y, Wong M, Barboza M, Lebrilla CB. Comprehensive structural glycomic characterization of the glycocalyxes of cells and tissues. *Nat Protoc*. 2020:**15**(8):2668–2704.

Lin RZ, Chang HY. Recent advances in three-dimensional multicellular spheroid culture for biomedical research. *Biotechnol J*. 2008:**3**(9–10):1172–1184.

Liu X, Hummon AB. Quantitative determination of irinotecan and the metabolite SN-38 by nanoflow liquid chromatography-tandem mass spectrometry in different regions of multicellular tumor spheroids. *J Am Soc Mass Spectrom*. 2015:**26**(4):577–586.

Neef SK, Janssen N, Winter S, Wallisch SK, Hofmann U, Dahlke MH, Schwab M, Murdter TE, Haag M. Metabolic drug response phenotyping in colorectal cancer organoids by LC-QTOF-MS. *Meta*. 2020:**10**(12).

Oh YJ, Dent MW, Freels AR, Zhou Q, Lebrilla CB, Merchant ML, Matoba N. Antitumor activity of a lectibody targeting cancer-associated high-mannose glycans. *Mol Ther.* 2022:**30**(4): 1523–1535.

Ozcan S, An HJ, Vieira AC, Park GW, Kim JH, Mannis MJ, Lebrilla CB. Characterization of novel *O*-glycans isolated from tear and saliva of ocular rosacea patients. *J Proteome Res*. 2013:**12**(3): 1090–1100.

Pang Z, Chong J, Zhou G, de Lima Morais DA, Chang L, Barrette M, Gauthier C, Jacques P-É, Li S, Xia J. MetaboAnalyst 5.0: narrowing the gap between raw spectra and functional insights. *Nucleic Acids Res*. 2021:**49**(W1):W388–W396.

Park DD, Xu G, Wong M, Phoomak C, Liu M, Haigh NE, Wongkham S, Yang P, Maverakis E, Lebrilla CB. Membrane glycomics reveal heterogeneity and quantitative distribution of cell surface sialylation. *Chem Sci*. 2018:**9**(29):6271–6285.

Park S-J, Lee J, Qi Y, Kern NR, Lee HS, Jo S, Joung I, Joo K, Lee J, Im W. CHARMM-GUI glycan Modeler for modeling and simulation of carbohydrates and glycoconjugates. *Glycobiology*. 2019:**29**(4): 320–331.

Park DD, Phoomak C, Xu G, Olney LP, Tran KA, Park SS, Haigh NE, Luxardi G, Lert-Itthiporn W, Shimoda M et al. Metastasis of cholangiocarcinoma is promoted by extended high-mannose glycans. *Proc Natl Acad Sci U S A*. 2020:**117**(14):7633–7644.

Pettersen EF, Goddard TD, Huang CC, Couch GS, Greenblatt DM, Meng EC, Ferrin TE. UCSF chimera—a visualization system for exploratory research and analysis. *J Comput Chem*. 2004:**25**(13): 1605–1612.

Raudvere U, Kolberg L, Kuzmin I, Arak T, Adler P, Peterson H, Vilo J. G:profiler: a web server for functional enrichment analysis and conversions of gene lists (2019 update). *Nucleic Acids Res*. 2019:**47**(W1):W191–W198.

Reily C, Stewart TJ, Renfrow MB, Novak J. Glycosylation in health and disease. *Nat Rev Nephrol*. 2019:**15**(6):346–366.

Ruhaak LR, Xu G, Li Q, Goonatilleke E, Lebrilla CB. Mass spectrometry approaches to glycomic and glycoproteomic analyses. *Chem Rev*. 2018:**118**(17):7886–7930.

Sethi MK, Fanayan S. Mass spectrometry-based *N*-glycomics of colorectal cancer. *Int J Mol Sci*. 2015:**16**(12):29278–29304.

Szklarczyk D, Gable AL, Lyon D, Junge A, Wyder S, Huerta-Cepas J, Simonovic M, Doncheva NT, Morris JH, Bork P et al. STRING v11: protein–protein association networks with increased coverage, supporting functional discovery in genome-wide experimental datasets. *Nucleic Acids Res*. 2018:**47**:D607–D613.

Takahashi M, Kuroki Y, Ohtsubo K, Taniguchi N. Core fucose and bisecting GlcNAc, the direct modifiers of the *N*-glycan core: their functions and target proteins. *Carbohydr Res*. 2009:**344**(12): 1387–1390.

Taki T, Takamatsu M, Myoga A, Tanaka K, Ando S, Matsumoto M. Glycolipids of metastatic tissue in liver from colon cancer: appearance of Sialylated Lex and Lex Lipids1. *J Biochem*. 1988:**103**(6): 998–1003.

Vidi PA, Bissell MJ, Lelievre SA. Three-dimensional culture of human breast epithelial cells: the how and the why. *Methods Mol Biol*. 2013:**945**:193–219.

Waterhouse A, Bertoni M, Bienert S, Studer G, Tauriello G, Gumienny R, Heer FT, de Beer TAP, Rempfer C, Bordoli L et al. SWISS-MODEL: homology modelling of protein structures and complexes. *Nucleic Acids Res*. 2018:**46**(W1):W296–w303.

Weigelt B, Ghajar CM, Bissell MJ. The need for complex 3D culture models to unravel novel pathways and identify accurate biomarkers in breast cancer. *Adv Drug Deliv Rev*. 2014:**69-70**: 42–51.

Wong M, Xu G, Barboza M, Maezawa I, Jin LW, Zivkovic A, Lebrilla CB. Metabolic flux analysis of the neural cell glycocalyx reveals differential utilization of monosaccharides. *Glycobiology*. 2020a:**30**(11):859–871.

Wong M, Xu G, Park D, Barboza M, Lebrilla CB. Author correction: intact glycosphingolipidomic analysis of the cell membrane during differentiation yields extensive glycan and lipid changes. *Sci Rep*. 2020b:**10**(1):21377.

Yang JM, Byrd JC, Siddiki BB, Chung YS, Okuno M, Sowa M, Kim YS, Matta KL, Brockhausen I. Alterations of *O*-glycan biosynthesis in human colon cancer tissues. *Glycobiology*. 1994:**4**(6): 873–884.

Yao K, Gietema JA, Shida S, Selvakumaran M, Fonrose X, Haas NB, Testa J, O'Dwyer PJ. In vitro hypoxia-conditioned colon cancer cell lines derived from HCT116 and HT29 exhibit altered apoptosis susceptibility and a more angiogenic profile in vivo. *Br J Cancer*. 2005:**93**(12):1356–1363.

Yue X, Lukowski JK, Weaver EM, Skube SB, Hummon AB. Quantitative proteomic and phosphoproteomic comparison of 2D and 3D colon cancer cell culture models. *J Proteome Res*. 2016:**15**(12): 4265–4276.

Zhao Q, Zhan T, Deng Z, Li Q, Liu Y, Yang S, Ji D, Li Y. Glycan analysis of colorectal cancer samples reveals stage-dependent changes in CEA glycosylation patterns. *Clin Proteomics*. 2018:**15**(1):9.

Zhou Q, Xie Y, Lam M, Lebrilla CB. *N*-Glycomic analysis of the cell shows specific effects of glycosyl transferase inhibitors. *Cell*. 2021:**10**(9):2318.

Zhu W, Ma L, Qian J, Xu J, Xu T, Pang L, Zhou H, Shu Y, Zhou J. The molecular mechanism and clinical significance of LDHA in HER2-mediated progression of gastric cancer. *Am J Transl Res*. 2018:**10**(7): 2055–2067.